Unravelling Heterodyne Force Microscopy
Verbiest, G.J.

Citation
Verbiest, G. J. (2013, November 19). *Unravelling Heterodyne Force Microscopy*. *Casimir PhD Series*. Retrieved from https://hdl.handle.net/1887/22238

Version:	Not Applicable (or Unknown)
License:	Leiden University Non-exclusive license
Downloaded from:	https://hdl.handle.net/1887/22238

Note: To cite this publication please use the final published version (if applicable).

Cover Page

Universiteit Leiden

The handle http://hdl.handle.net/1887/22238 holds various files of this Leiden University dissertation

Author: Verbiest, Gerard Jan
Title: Unravelling heterodyne force microscopy
Issue Date: 2013-11-19

CHAPTER 6

Contrast Mechanism in Heterodyne Force Microscopy:
Friction at Shaking Nanoparticles

To pinpoint the physical mechanism that is responsible for the contrast forma-tion in Heterodyne Force Microscopy, we perform a quantitative analysis, in which we compare our experimentally observed contrasts with simulations and calculations. Firstly, we show that the contrasts greatly depend on both the ap-plied contact force and on the precise ultrasonic excitation scheme used. Our analysis shows that we can rule out Rayleigh scattering, variations in sample (visco)elasticity, damping of the ultrasonic tip motion, and ultrasound attenu-ation in the nanoparticles and finally have to conclude that friction at shaking nanoparticles is the only remaining physical contrast formation mechanism. We find additional evidence for this mechanism in an estimate of the involved energy dissipation.

6.1   Introduction

HFM measurements showed the capability to image subsurface features with remarkable contrast and lateral resolution [3, 6–15]. It is claimed that one can image gold nanoparticles with a diameter of $\sim$ 17.5 nm buried at a depth of 500 nm in a polymer [6]. The lateral resolution in these images is surprising, since it is equal to the diameter of the gold nanoparticles. Maybe even more surprising is the generated contrast, which clearly exceeds the variations in the background of the images, although the size of the nanoparticles is only a fraction of the thickness of the sample.

Unfortunately, none of the published HFM experiments provide quantitative information on the measured amplitude and phase range, on the applied contact force during the measurement, and on the precise excitation scheme in combination with the resonance frequencies of the cantilever. Also, the actual depth of the subsurface features is confirmed only in one publication with an independent technique [15]. This makes it difficult, if not impossible, to understand the contrast formation mechanism.

Only Cantrell et al. provide quantitative information on the nanoparticle size, the depth, the resolution, and the contrast [8]. Measured above gold nanoparticles that have a diameter of 15 nm and that are buried at a depth of 7 μm, they obtain a subsurface phase contrast of $\sim$ 2.5 degrees and a resolution of 25 nm. However, the published image is exaggerated in contrast such that it discriminates only 2 levels, which leaves questions about a proper identification of the nanoparticles.

Considering the wavelengths of the ultrasonic excitations, it is hard to understand the reported contrast and resolution. The wavelength of the ultrasonic sample excitation is of the order of mm's, which is much larger than the size of the subsurface nanoparticles (nm's) and their depth below the surface (up to μm's). As a consequence, the measurements are performed in near-field and one expects the obtainable resolution to be equal to the depth of the nanoparticles. This argument holds only, if the physical contrast mechanism is based on the usual, wavelike propagation of the ultrasonic wave that is sent into the sample. Therefore, it is of crucial importance to understand the physical contrast formation mechanism. Equipped with this knowledge, it might also be possible to understand the remarkable resolution of reported HFM experiments.

It is difficult to pinpoint the dominating physical contrast mechanism, as it involves the ultrasound propagation within the sample, the cantilever dynamics, nonlinear mixing, resonance frequency shifting, the explicit excitation scheme, the resonance frequency spectrum of the cantilever, and the response to variations in the tip-sample interaction, which are determined by the local elasticity and adhesion of the sample. All these factors can significantly change the heterodyne signal leading to a measurable contrast. Due to recent progress

in exactly these issues (see *all* previous chapters and [28, 42, 52, 69]), it is now possible to perform a detailed study on the contrast formation mechanism in Heterodyne Force Microscopy.

In this chapter, we present a full quantitative analysis on all possible, physical mechanisms to explain our experimentally observed contrast on a well characterized sample. We show that Rayleigh scattering (see Chap. 2 and [28]) is not the dominating contrast mechanism, as the experimentally observed contrasts are orders of magnitude larger. Then, we explicitly calculate the cantilever dynamics for different tip-sample interactions and show that variations in sample elasticity indeed lead to a contrast that is comparable in magnitude to the experiments. However, the derived amplitude contrast is inverted with respect to the experimentally observed one such that we can rule out also elasticity variations as the sole reason for the contrast. The only remaining possibility is tip-sample damping. As we can exclude also tip damping (see Chap. 4 and [52]), we are left with sample damping and finally conclude that *friction* at *shaking* nanoparticles must be the responsible physical mechanism for the contrast. We find additional evidence for this mechanism in an estimate of the involved energy dissipation. From our analysis it becomes clear that the contrast in an HFM measurement strongly depends on the applied contact force as well as on the precise ultrasonic excitation scheme applied with respect to the resonance frequencies (and their shifts) of the cantilever.

6.2 The Detection of Deeply Buried Gold Nanoparticles with a HFM

For our study, we prepared a sample consisting of the following layers (from bottom to top): a Silicon wafer with native oxide, a ~ 97 nm thick PMMA layer, a 30 nm thick PVA layer with embedded gold nanoparticles (diameter 20 nm), and a 82 nm thick PVA top layer. The density of the gold nanoparticles is 0.7 ± 0.6 particles/μm^2. The precise sample preparation as well as its characterization, in which we even determined the depth of the Au nanoparticles with an independent measurement based on Rutherford backscattering, are described in detail in Appxs. 6.A and 6.B.

In our HFM experiment, we chose the ultrasonic excitation frequencies of both the tip and the sample as well as the difference frequency *off* resonance, i.e. not on (or within the width) of a resonance peak of the cantilever. In analogy to Sect. 1.2, we call this excitation scheme *off-off resonance*. The first *on/off* indication describes whether f_{diff} (heterodyne signal) is tuned to a resonance frequency of the cantilever, whereas the second *on/off* indication describes whether f_t (ultrasonic tip excitation) is tuned to a resonance. This leads to four different excitation schemes.
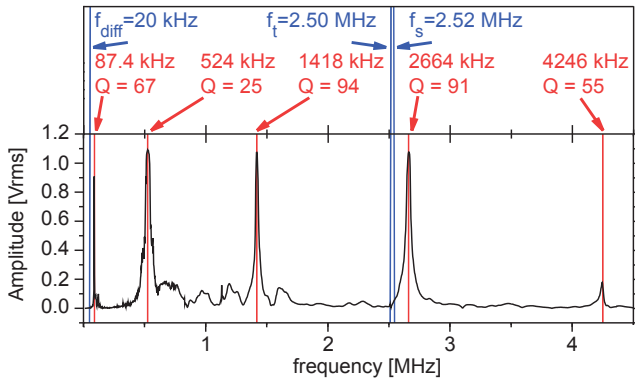
Figure 6.1: The HFM excitation scheme (*off-off resonance*) with respect to the vibration spectrum of the free hanging cantilever. A red line indicates a resonance frequency: its value and corresponding Q-factor are indicated in the top panel. The blue lines indicate the applied excitation frequencies of the tip $f_t = 2.50$ MHz, the sample $f_s = 2.52$ MHz, and the difference frequency $f_{\text{diff}} = 20$ kHz.

Figure 6.1 shows the excitation scheme and the vibration spectrum of the free hanging cantilever, of which we calibrated the spring constant to be 2.7 N/m using the thermal noise method [67]. Using the method described in Chaps. 4 and 5 as well as [52,69], we determined the ultrasonic tip amplitude to be $A_t = 1.34$ nm and the ultrasonic sample amplitude to be $A_s = 0.37$ nm.

In the HFM experiment, shown in Fig. 6.2, we simultaneously measured the height, the amplitude A_{diff} and the phase ϕ_{diff} of the difference frequency f_{diff} for various contact forces F_c. Feedback was performed in contact mode operation. The contact force F_c is decreased from top to bottom: 163 nN, 115 nN, 67 nN, and 2.4 nN. The gold nanoparticles are visible in all channels at $F_c = 163$ nN. The observed density of 1.2 particles/μm^2 fits the independently determined density. Most of the gold nanoparticles are still visible at $F_c = 115$ nN, although the contrasts are significantly reduced. At lower force, we do not detect any nanoparticles in any of the channels, which supports that the gold nanoparticles are indeed fully buried under a 82 nm thick PVA layer. Considering the indentation depths, see Fig. 6.2, and the thickness of the PVA top layer, we have to conclude that the gold nanoparticles are only visible by poking hard enough into the sample, although it is striking that we see them at all in the height images. At $F_c = 2.4$ nN, we start probing the attractive part of the tip-sample interaction and recognize that we have damaged the surface, while measuring at the higher contact forces. This observation
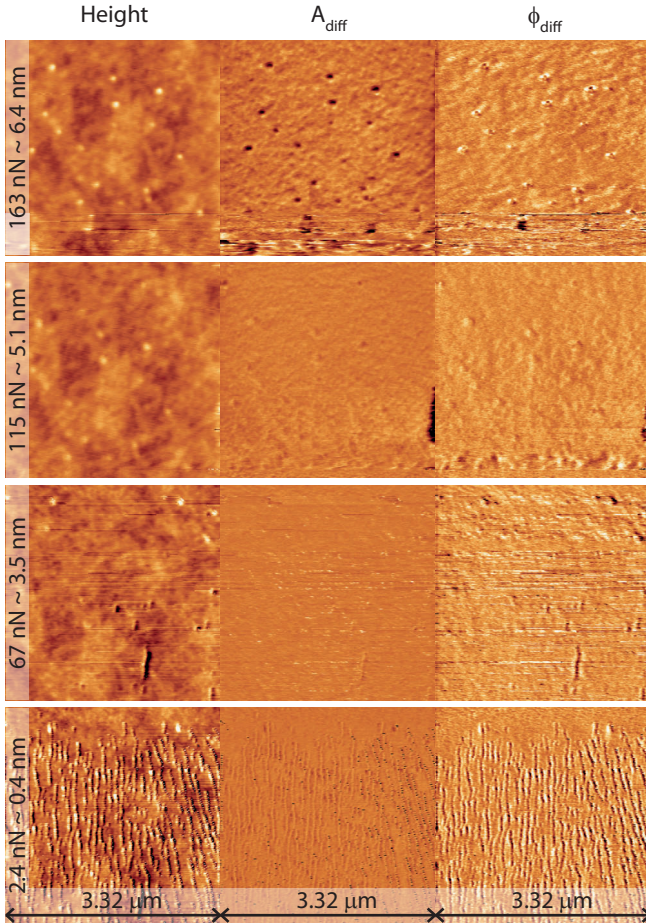
Figure 6.2: From left to right measured simultaneously: the height and both the amplitude A_{diff} and the phase ϕ_{diff} of the difference frequency. The contact force F_c as well as the resulting average indentation into the sample are indicated at the left in the height images. The gold nanoparticles are only visible at a contact force of 163 nN and 115 nN. At these forces, they are not only visible in the subsurface channels, but also in the height image. We 'lose' the nanoparticles in all three channels with decreasing force. At a $F_c = 2.4$ nN, we observe that we damaged the surface, while measuring at the higher forces. All images within one channel do have the same (color) range such that the contrast for different contact forces can be compared directly. We provide typical cross sections with absolute values of the three channels at the positions of the nanoparticles in Appx. 6.C. $A_s + A_t = 1.71$ nm.

contradicts the general belief that Heterodyne Force Microscopy provides a

truly nondestructive way of imaging buried features: large indentation might damage soft biological samples. Finally, one might question the purpose of an HFM with its complicated excitation scheme and electronics as well as the use of ultrasound, if the desired information is also present in the height images.

Before we discuss the contrast at $F_c = 2.4$ nN, it is important to understand the lateral friction in HFM experiments. It has been shown by Dinelli et al. [70] that the lateral friction in UFM measurements almost vanishes, if the cantilever is not in contact with the sample during a part of its high frequency oscillation. In most HFM experiments, the cantilever is getting in and out of contact with the sample. Therefore, the reduction of the lateral friction is also expected to occur in HFM. In our HFM measurements at the high contact forces (163 nN, 115 nN, and 67 nN), the cantilever is always *fully* in contact with the sample during the *complete* high frequency motion. Therefore, at these contact forces, the lateral friction is not reduced, which might have led to a damaged sample. In contrast, at $F_c = 2.4$ nN, the cantilever is not in contact with the sample during a significant part of the high frequency motion (compare $A_s + A_t = 1.71$ nm with the indentation of 0.4 nm). As a consequence, we can exclude any lateral frictional effects in the images at this contact force. As this image at $F_c = 2.4$ nN was measured after the images at higher contact forces , we have to conclude that the sample was indeed damaged while measuring at the higher contact forces (see the vertical lines). We did not see any damage in the image at higher contact forces as the tip was pushed deeper into the sample than the height corrugations, which resulted from the damage (compare the indentation of at least 3.5 nm with the height corrugations of 1.5 nm).

At $F_c = 2.4$ nN, both subsurface channels (amplitude and phase) show a clear correlation with the height. As the cantilever mainly probes the attractive part of the tip-sample interaction during an oscillation cycle, the effective contact area of the tip depends on the height variations of the sample: the contact area is much smaller on a mountain than in a valley. Adhesion is directly proportional to the contact area. Based on the analytical derivation of the heterodyne signal (see Chap. 5 and [69]), we expect that adhesion variations indeed lead to a variation in both the amplitude and the phase of the subsurface signal. We attribute the strong correlation, with its stripy pattern, between the height and the subsurface channels to a variation in contact area, which leads to different values for the adhesion in the tip-sample interaction, and conclude that variations in the adhesion can generate a contrast in the subsurface channels.

To quantify the contrasts of the gold nanoparticles in Fig. 6.2, we provide the average values above the nanoparticles for the different channels with respect to their background. To enable a comparison with the expected contrast based on Rayleigh scattering (see Chap. 2 and [28]), we have to normalize the amplitudes A_{diff} with respect to their background amplitudes A_b. At $F_c = 163$

nN, the height is 2.8 nm, the amplitude A_{diff} is -120 pm, the background amplitude A_b is 270 nm, the normalized amplitude contrast -0.44, and the phase ϕ_{diff} is 7.2 degrees. At $F_c = 115$ nN, the normalized amplitude contrast is -0.11 and the phase contrast is 2.9 degrees, see also Tab. 6.1. Based on Rayleigh scattering, the expected normalized amplitude contrast is 10^{-6} and the phase contrast is 0.1 millidegree for a gold particle with a diameter of 20 nm buried 50 nm deep under a polymer (PMMA) (see Chap. 2 and [28]). It is striking that the experimentally observed normalized amplitude contrast is 5 orders of magnitude larger and the experimentally observed phase contrast is 4 orders of magnitude larger than the theoretically predicted ones. We have to conclude that Rayleigh scattering does *not* form a major contribution to the physical contrast mechanism in current HFM measurements at MHz frequencies.

6.3 Subsurface Contrast due to Variations in the Tip-Sample Interaction

In Chap. 5 and [69] it was elucidated how the heterodyne signal is generated: its magnitude strongly depends on both the applied contact force and the specific characteristics of the tip-sample interaction. In the appendices, we show, both experimentally (Appx. 6.D) and analytically (Appx. 6.E), that the heterodyne signal depends on the elastic properties of the sample, which is characterized by the Young's modulus E. For sufficiently soft samples, the amplitude A_{diff} of the heterodyne signal is proportional to E. Therefore, we consider in the following elasticity variations in the sample, due to the presence of the nanoparticles, as a possible physical contrast mechanism.

From an analytical 1D model, we estimate that the Young's modulus above a gold nanoparticle is $\sim 10\%$ higher than the Young's modulus of PVA, which is 2.4 GPa, see Appx. 6.F. The $\sim 10\%$ elasticity variation should be easily detected with Force Modulation Microscopy and Ultrasonic Force Microscopy. Therefore, both techniques should be able to *see* the nanoparticles. In principle this questions the application of Heterodyne Force Microscopy. However, we will see that a different physical contrast mechanism, which can neither be studied with Force Modulation Microscopy nor with Ultrasonic Force Microscopy, dominates the contrasts in this particular HFM experiment. To determine the contrast formation based on these elasticity variations, we numerically calculated the motion of the cantilever for different tip-sample interactions using the method outlined in Chap. 3 and in [42]. Although our numerical calculation shows a hysteresis between the approach and the retract curve of the cantilever, in this chapter, for reasons of clarity, we show only the results for the approach curves. We did, however, calculate both sets of curves and found that the difference in contrast is negligible between a determination from the approach or retract curves, respectively. To receive an upper bound on the

contrast and to elucidate the contrast formation effect on the basis of small
elasticity variations, we consider Young's moduli up to 6 GPa.

For the simulations, we fitted an experimentally obtained tip-sample inter-
action F_{ts} measured on PMMA with the Derjaguin-Muller-Toporov (DMT-)
model, see Sect. 1.4 and [23]. We used this description of F_{ts} for the 2.4 GPa
case and modified only the elasticity for the other cases describing samples with
Young's moduli of 2, 3, 4, 5, and 6 GPa, respectively. A parameter called λ,
which is related to the elasticities of the tip and the sample, is usually used
to differentiate between the applicabilities of different models that describe the
tip-sample interaction, see Fig. 1.8 and [27]. As $\lambda = 0.63$ in our case, one
should use the Maugis-Dugdale (M-D-) model, see Fig. 1.8 [25]. Nevertheless,
our approach with the DMT-model is fully justified, as we have demonstrated
in Chap. 4 and in [52] that it does not matter at all for the numerical simula-
tions which of the models describes the tip-sample interaction, as long as the fit
perfectly matches the (experimentally obtained) tip-sample interaction. The
only thing that matters is the particular shape (form) of $F_{ts}(z)$ and *not* the
model that is used to describe this particular interaction. In addition, please
note that it is almost impossible to use the M-D-model, as it does not provide
an analytical expression for F_{ts} such that it can only be solved iteratively, if
the value of λ is not known a priori.

As the specific vibration spectrum of the cantilever has great influence on
the results, we first matched the spectrum used in the calculations to that of
our experiment, see Appx. 6.G. To elucidate the effect of different ultrasonic
excitation schemes, we considered three distinct cases, which all three had a
difference frequency at 20 kHz (well below the first resonance frequency of the
cantilever). This implies that the first *on/off* indication is always *off* in our
case. In the *off-off resonance* case both ultrasonic excitations are chosen *off*
resonance halfway between the 3rd and 4th resonance of the cantilever. In the
off-on resonance case the excitation of the tip coincides with the 4th resonance
of the cantilever and the sample frequency is 20 kHz below it. The *experimental
excitation* scheme reflects the particular situation of our experiment as shown
in Fig. 6.1, which has both ultrasonic excitations off resonance but relatively
close to the 4th resonance. The other excitation schemes are depicted in Appx.
6.H.

Considering Young's moduli between 2 and 6 GPa as well as the *experimen-
tal excitation* scheme, Fig. 6.3 shows the corresponding tip-sample interactions
and, as a function of the applied contact force, the indentations as well as the
amplitudes A_{diff} and phases ϕ_{diff} of the heterodyne signal at the difference
frequency. The results of the other two excitation schemes are provided in
Appx. 6.H. The contrasts at a certain contact force can now be evaluated
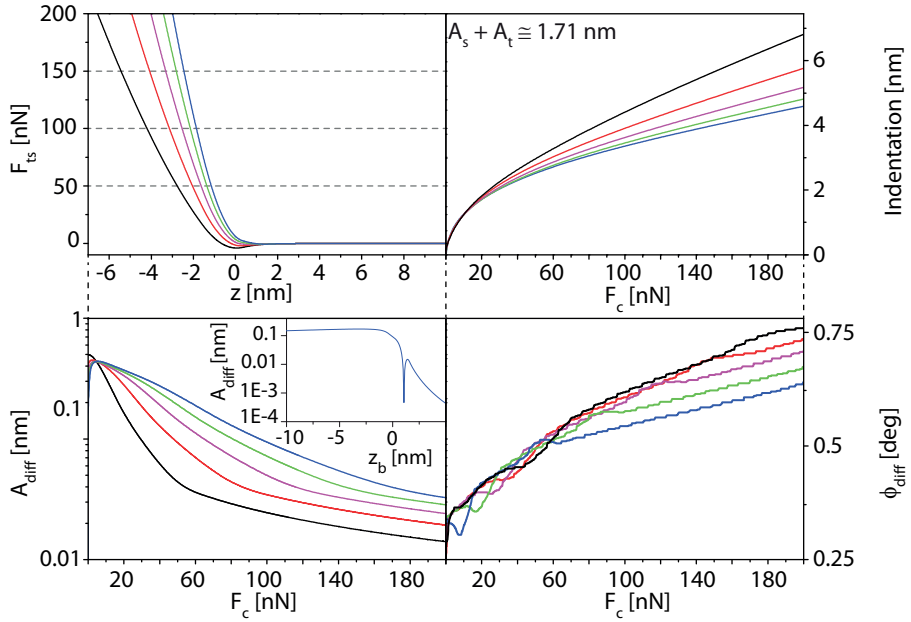from the difference in the signals stemming from different elasticities. The

Figure 6.3: Considering the *experimental excitation* scheme, we calculated the tip-sample interaction $F_{ts}(z)$ and, as a function of the applied contact force F_c (given by I_0), the corresponding sample indentation as well as the amplitude A_{diff} and phase ϕ_{diff} of the heterodyne signal for different sample elasticities: 2 GPa (black), 3 GPa (red), 4 GPa (magenta), 5 GPa (green), and 6 GPa (blue). The inset in the lower left panel shows A_{diff} for 6 GPa plotted as a function of the height of the cantilever's base, z_b, such that a comparison becomes possible with other calculations (see Chaps. 3, 4, and 5, as well as [42, 52, 69]).

indentation contrast decreases with decreasing contact force. The amplitude contrast stays over a large range almost constant (and even increases), before it collapses to zero at very small contact forces. The phase contrast strongly depends on the specific excitation scheme, but always collapses to zero at very small contact forces.

To receive upper bounds, we determine the contrasts from the differences between a sample with 2 GPa and 6 GPa. In Tab. 6.1, we list the results for the different excitation schemes as well as the experimentally determined contrasts for comparison. For completeness, we provide, for the *experimental* scheme, also the contrasts obtained from the difference in samples with 2.4 GPa (PVA) and 2.6 GPa (effective elasticity above the nanoparticles, as derived in Appx. 6.F). Starting with the height contrast, we find comparable values between the experiment and the calculated excitation schemes, except for the *experimental*

scheme, in which the contrast is obtained from the difference in samples with
2.4 GPa (PVA) and 2.6 GPa.

The decrease in height contrast for smaller contact forces is reproduced for
all cases. Considering the amplitude contrast ΔA_{diff}, the absolute values in
the experiment are between a factor 1 and 100 times larger than the calculated
ones. There are three striking issues, if one compares the different ΔA_{diff} values
in more detail. Firstly, the values of the *off-on resonance* case are significantly
lower than all other values. This is due to this particular excitation scheme
(see also Appx. 6.I), in which the ultrasonic tip amplitude is significantly
decreased when the cantilever gets into contact with the surface, due to the
related frequency shift of the 4th resonance. The size of this shift and, there-
fore, also of the amplitude reduction of the ultrasonic tip vibration, increases
both with increasing contact force and with the stiffness of the sample. The
off-on resonance case is a special excitation scheme and its particular behavior
is (almost) not present in the *off-off resonance* case and in the *experimental
excitation*. This is also the reason why the values of the latter schemes are com-
parable. Secondly, in contrast to the experiment, where the ΔA_{diff} contrast is

method	$F_{contact}$ [nN]	height [nm]	ΔA_{diff} [pm]	A_b [pm]	A_c []	$\Delta\phi_{\mathrm{diff}}$ [deg]
experiment	**163**	**2.8**	**-120**	**270**	**-0.44**	**7.2**
	115	**1.2**	**-40**	**360**	**-0.11**	**2.9**
off-on resonance	163	1.8	-0.86	7.0	-0.12	11
($2 \rightarrow 6$ GPa)	115	1.2	-0.23	9.6	-0.02	12
off-off resonance	163	1.8	42	20	2.1	0.014
($2 \rightarrow 6$ GPa)	115	1.3	63	24	2.6	-0.002
exp. scheme	163	1.8	17	15	1.1	0.120
($2 \rightarrow 6$ GPa)	115	1.2	32	19	1.7	0.083
exp. scheme	163	0.08	0.87	17	0.05	0.027
($2.4 \rightarrow 2.6$ GPa)	115	0.03	1.1	21	0.05	0.008

Table 6.1: The obtained contrasts in the height, the amplitude A_{diff}, the normalized
amplitude A_c (for which we also provide the background amplitude A_b), and the
phase ϕ_{diff} for a contact force of 163 nN and 115 nN. The contrasts are provided for
the experiment as well as for different numerical calculations, in which we take into
account specific exaction schemes. To receive clear upper estimates, we determined
(most of) the contrasts from the differences in the curves between a sample with 2
GPa and 6 GPa. For completeness, we provide, for the *experimental* scheme, also the
contrasts obtained from the difference in samples with 2.4 GPa (PVA) and 2.6 GPa
(effective elasticity above the nanoparticles, as derived in Appx. 6.F).

less for a lower contact force, the *off-off resonance* case and the *experimental* schemes show a larger contrast at lower force. This already indicates a problem. However, the most striking issue is the sign of the contrast. In the experiment we have a negative amplitude contrast ΔA_{diff}, whereas it is positive for the *off-off resonance* and the *experimental* schemes. Whatever the argument is, the elasticity (or viscoelasticity) above the nanoparticle is for sure *increased*, which leads to a *higher* amplitude A_{diff} (see Fig. 6.3) and to a *positive* amplitude contrast ΔA_{diff}. We have to conclude that, although variations in the elasticity produce a contrast with a magnitude that is comparable with the experiments, elasticity variations cannot explain the inverted contrast. A different physical mechanism must be present.

The contrast inversion in the *off-on resonance* case is due to the larger frequency shift of the 4th mode on stiffer samples. Above the nanoparticle, the amplitude reduction of the ultrasonic tip vibration A_t is significantly larger than the reduction on the PVA without nanoparticles (see the details in Appx. 6.I). The contrast inversion in this case indicates the importance to provide both the precise excitation scheme and the spectrum of the cantilever for each published HFM measurement.

The more proper value for a comparison between the experiment and the calculated schemes, is the normalized amplitude contrast A_c. Ignoring the minus sign, we find values of the right order of magnitude. The values of the simulated *experimental* schemes are only a factor ~ 3 times too high, which has to be compared to Rayleigh scattering that predicts an A_c that ~ 100000 times too low.

The magnitude of the experimentally observed phase contrast $\Delta\phi_{\mathrm{diff}}$ is only comparable to the special case of the *off-on resonance* excitation scheme. The large phase shift in this scheme is due to the frequency shift of the 4th resonance: the particular *off-on resonance* excitation scheme makes the tip vibration especially sensitive to phase changes based on frequency shifts (see Appx. 6.I). Although much smaller in magnitude, a similar argument holds also for the phase shifts in the *off-off resonance* and *experimental excitation* schemes. Since the ultrasonic tip excitation in the *experimental* scheme is closer to the 4th resonance frequency of the cantilever, we observe a larger phase contrast than in the *off-off resonance* scheme.

We conclude that the contrast from (small) variations in the elasticity of the sample results in a much larger contrast than Rayleigh scattering. The order of magnitude is comparable to the contrast measured in the experiments. However, variations in sample elasticity *cannot* be the physical contrast mechanism in our HFM experiment, as it would imply an *opposite* sign.

6.4   Friction at Shaking Nanoparticles

Ruling out both variations in the tip-sample interaction (elasticity and adhesion) and Rayleigh scattering, the only remaining physical contrast mechanism must lead to a significant reduction of the tip amplitude A_t or sample amplitude A_s above the nanoparticles, as $A_{\mathrm{diff}} \sim A_t A_s / \sqrt{A_t^2 + A_s^2}$ (see Chap. 5 and [69]). These reductions can be described as tip-sample damping. Tip damping can also be excluded, as it has been shown that A_t keeps 99.7% of its amplitude at a contact force of 25 nN even on a hard sample like Silicon (see Chap. 4 and [52]). One should mention here that the damping of the resonance frequencies of a cantilever that is in contact with a sample, is generally assumed to be directly proportional to the Young's modulus of the sample [71]. Without significant tip damping, the contrast must be due to a reduction in the sample amplitude. Since a reduction of A_s, due to tip-sample damping, is expected to occur also on the polymer without nanoparticles, and since A_{diff} is larger above the nanoparticle, due to the increase in the effective Young's modulus, we need a mechanism that leads to a strong decrease of A_s only above the nanoparticle to overcompensate the increase in A_{diff} such that it effectively leads to a contrast inversion. In the following we consider different possibilities.

Let us start with a possible vertical motion of the nanoparticles in the polymer matrix. At low ultrasonic sample frequencies, this motion is surely in phase with the excitation. However, if the ultrasonic excitation is above the resonance frequency of the system "nanoparticle in polymer", the motion will be out of phase. This would indeed lead to a significant reduction of A_s only above the nanoparticle. The problem, however, is that the sample excitation is at 2.5 Mhz and that we estimated the resonance frequency of the "nanoparticle in polymer" system to be ~ 9 GHz. The nanoparticles should, therefore, simply follow the ultrasonic displacements of the polymer.

Another mechanism worth considering is sample damping (reduction of A_s) by energy dissipation at the nanoparticles. Next to the contrast formation based on pure energy dissipation, a temperature effect might additionally enhance the contrast, especially if, e.g., the elasticity of the polymer would have a strong dependence on the temperature. To evaluate this effect, we estimate the energy dissipation from the experiment. We determine the sample amplitude A_s (far away from the nanoparticle) in analogy to the method described in Chap. 3 and in [42]. With $A_s \sim 0.22$ nm at $F_c = 163$ nN, we need a reduction of $\sim 41\%$ to explain the observed contrast. A_s is ~ 0.29 nm at $F_c = 115$ nm and we need a reduction of $\sim 13\%$ to reach the corresponding contrast. Both estimations deliver a similar value: 0.83 and 0.37 pW, respectively. Therefore the maximum energy dissipation of the nanoparticles is in the order of 2.07 eV/oscillation of the ultrasonic sample vibration. This value is so small that we rule out also any temperature effects. It is important to realize here that the

local elastic response of the sample above the nanoparticles is increased (see Sect. 6.F), which leads according to Eq. 6.9 to an increased amplitude A_{diff} of the heterodyne signal even without considering any form of energy dissipation. As we observe holes, the real dissipation must be even higher and we estimate the additional dissipation (on the basis of the effective elasticity increase) to be in the order of 0.09 eV/oscillation. The real dissipation has, therefore, to be increased with this value. The remaining question is the physical mechanism that is responsible for this energy dissipation. One might consider ultrasound attenuation within the nanoparticles as well as friction at the interface between the nanoparticle and the polymer.

The ultrasound attenuation for gold is ~ 150 times smaller than the attenuation for PVA. Therefore the total energy dissipation is less at the positions measured above the nanoparticles than at the positions far away from them. This effect results, in comparison to the experiment, again in a wrong sign of the contrast, as A_s would be larger above the nanoparticles. We estimate the resulting energy 'gain' based on a smaller ultrasound attenuation at the nanoparticles to be 0.45 eV/oscillation. The real dissipation that is responsible for the contrast, must be increased with this value to overcompensate the contrast inversion.

We are left with friction at the interface between the nanoparticles and the PVA. Due to a weak (chemical) bonding between the gold and the PVA, the nanoparticles might slip instead of following the displacements of the PVA. One might even consider a small cavity around the nanoparticles such that they are *shaken* up and down. Both effects would lead to a significant amount of friction. Considering *shaking* nanoparticles, we are able to explain our observed contrast with a total energy dissipation of 2.61 eV/oscillation at the nanoparticles. This value is comparable (and definitely in the right order of magnitude) with the energy dissipation derived from atomic scale friction experiments of a sharp tip in contact with a surface [72].

Pinpointing the physical mechanism to friction at *shaking* nanoparticles, we can consider the consequences for the lateral resolution. If one assumes that the propagation in amplitude reduction obeys a scattering-like behavior, the 'fingerprints' of the nanoparticles at the surface should show a larger diameter than the diameter of the nanoparticles. Moreover, as we are measuring in near-field, the size of the 'fingerprints' should be in the order of the depth of the nanoparticles. The deeper the nanoparticle is, the larger should be its image at the surface. These considerations stand in clear contrast to experimental observations: nanoparticles with a diameter of ~ 17.5 nm, buried 500 nm deep, are imaged with a diameter of ~ 20 nm [6], and the imaged diameter is even decreasing with increasing depth of the nanoparticles [15]. A solution to this might be found by considering a combination of a stress field that is introduced on the nanoparticle by the indenting tip [29,30], a resulting *shaking*

that is no longer parallel to the initial ultrasonic displacements of the PVA, and a highly nonisotropic propagation of the amplitude reduction such that there is a significant enhancement in the direction of the *shaking* movement.

6.5   Conclusions

In conclusion, we presented a first quantitative analysis of the contrast formation mechanism of an HFM experiment. We showed that the contrasts strongly depend on the applied contact force, which raises serious questions about the general conception of measuring *nondestructively* with an HFM. Elucidating the physical contrast mechanism, we showed that Rayleigh scattering is not dominating, as the contrast values are orders of magnitudes too small. Anyhow, Rayleigh scattering might become significant in the future with increasing frequencies of the ultrasonic excitations. Variations in the tip-sample interaction do generate a contrast that is significantly larger than predicted by Rayleigh scattering, and the magnitude is also comparable to the experimental values. This is valid for rather small variations in both the (visco)elasticity and, not shown here, also the adhesion. However, we can also rule out this contrast formation mechanism, as there is a problem with the sign that leads to contrast inversion. The only left over possibility is tip-sample damping. We showed that tip damping is not an issue and considered several effects for sample damping. Finally, we conclude that *friction* on *shaking* nanoparticles is the only remaining contrast formation mechanism. We receive additional evidence for this effect, as the energy dissipation estimated from the experiments fits well with the dissipation reported for atomic scale friction experiments. *Friction* on *shaking* nanoparticles can also explain the observed lateral resolution, if the reduction in sample amplitude is almost only in the direction, in which the nanoparticles are shaking.

Based on the new insight, we expect that the contrast mechanism differs greatly between the systems "nanoparticles in polymers" and "(gas) voids in a solid". In the latter, friction cannot be the dominating physical contrast mechanism, as the dissipated energy on the interface between a (gas) void and a solid is orders of magnitude lower than on the interface between a metal and a polymer. Therefore, we rather expect elasticity variations in the sample to dominate this contrast: a PVA nanoparticle with a radius of 10 nm inside a 209 nm thick gold plate results, according to Eq. 6.16, in a reduction of the effective elasticity by 75%. As a consequence, the difference amplitude A_{diff} is reduced with 2.5% above the PVA nanoparticle (see Eq. 6.9), which can easily be detected with a HFM. Future detailed quantitative research is needed that addresses the differences between these two systems with respect to the remaining questions.

Finally, we would like to stress that the observed contrast and resolution depend on many specific details of the experiment, as outlined in this chap-

ter. This includes even the possibility for a contrast inversion. Therefore, it is necessary to provide not only the amplitude and phase range of reported HFM measurements, but also the applied contact force, the particular excitation scheme, the frequency spectrum of the cantilever up to a resonance frequency higher than the highest applied ultrasonic frequency, and the ultrasonic amplitudes of both the tip/cantilever and the sample.

Appendices of Chapter 6

Materials and Methods

In the Supplementary Material, we provide necessary specific details, background information, and insight in our estimations and calculations to support the statements and results of Chap. 6.

We describe the precise details of the sample preparation in Appx. 6.A, and we present a detailed sample characterization by means of Rutherford Backscattering in Appx. 6.B. In Appx. 6.C, we provide typical cross sections of the HFM images (including the height channel) that are presented in Sect. 6.2, at the position of a gold nanoparticle. In Appx. 6.D, we show experimental evidence for the statement that a harder surface results in an increased amplitude of the signal at the heterodyne difference frequency. In Appx. 6.E, we even provide an analytical argument for this. Important for the correct determination of the expected contrasts, we derive, in Appx. 6.F, an upper bound on the elasticity variations induced by the buried gold nanoparticles in our sample. In Appx. 6.G, we describe how we set up our numerical calculations such that they match the conditions of the experiments as closely as possible, and, in Appx. 6.H, we provide a complete overview on the results of our simulations. Finally, in Appx. 6.I, we address the consequences of frequency shifts for the particular contrast formation.

6.A Sample Preparation

Inspired by the sample with buried gold nanoparticles of Shekhawat and Dravid [6], we set out to produce comparable ones. We decided to use gold nanoparticles with a diameter of 20 nm ($\pm10\%$), which we got from BBI Solutions [73]. A schematic cross section of the final sample that we used in the current study, is shown in Fig. 6.4. In the following, we describe important issues of the sample preparation and provide the recipe.

As a substrate, we used a freshly with acetone cleaned Silicon (100) wafer that was covered with a native oxide. The polymer layers (including the suspension with the nanoparticles) were deposited by means of a spin coater, see also the recipe below. We decided to use two different polymers: polymethylmethacrylaat (PMMA) with a degree of polymerization of 970 and polyvinyl alcohol (PVA) with a degree of polymerization of 2700. The degree of polymerization is the number of monomers in the molecule and it characterizes the length of a single polymer molecule. This information is important, as the material properties of the polymer layers strongly depend on the molecule length. As we faced some problems with clustering of the nanoparticles as well as with their density, we describe these issues shortly in the following. Our first attempt to create a
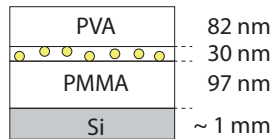
Figure 6.4: A schematic cross section of the final sample that we used in the current study. On the Silicon wafer, we have (from bottom to top), a 97 nm PMMA layer, a 30 nm PVA layer that also contains gold nanoparticles with a diameter of 20 nm, and a 82 nm PVA layer.

layer of gold nanoparticles on top of a spin coated PMMA layer was to let a suspension of pure (Milli-Q) water with gold nanoparticles evaporate at ambient conditions. This led to large "mountains" of clustered nanoparticles, which we measured with an Atomic Force Microscope (AFM). In our second attempt, we tried to *embed* the gold nanoparticles within a PVA layer by dissolving them in a PVA solution before spin coating on top of the PMMA. The gold nanoparticles did stick out with their "heads" just above the PVA layer, with which they were simultaneously spin coated, such that we easily could verify the density, again, with AFM. This approach resulted in an (for our research) unsuitable low density of nanoparticles of less than 0.1 nanoparticle/μm^2. By increasing the concentration of the nanoparticles in the PVA solution, we were able to increase the density to 0.7 ± 0.6 nanoparticle/μm^2. We derived this distribution from AFM measurements, see Fig. 6.5A. Finally, we buried the nanoparticles by spinning another PVA layer on top of this structure. As we considered that the solvent, which is present while spinning the additional PVA layer, might (partially) dissolve the thin nanoparticles/PVA layer that is to be buried, leading to a possible redistribution of the nanoparticles, we counterchecked the density with a Secondary Electron Microscope (SEM) on the final sample with the top PVA layer. Due to the different electron emissions between gold and PVA, the SEM is capable of imaging the nanoparticles, even if they are buried under a 82 nm thick PVA layer, see Fig. 6.5B.

The final recipe for the sample production is as follows:

1. solution: 30 mg PMMA / mL Toluene
   This results in a $\sim$ 97 nm thick PMMA layer, which was confirmed independently with an AFM measurement [74].

2. solution: 250 μL of 2 mg PVA / mL water + 750 μL suspension of pure water and gold nanoparticles
   This leads to a PVA layer with embedded gold nanoparticles with a diameter of 20 nm. The thickness of this PVA layer is less than 30 nm ($\sim$ 10 nm), as we verified with AFM that the "heads" of the gold nanoparticles

are sticking out. After burying this PVA layer with the top PVA layer,
we find an effective thickness of 30 nm for this layer that contains the
nanoparticles.

3. solution: 2mg PVA / mL water
   This step leads to a $\sim$ 82 nm thick PVA layer.

Each step in the recipe represents an individual spin coating procedure. In
each spin coating step, a droplet of the corresponding solution was put onto
the sample by means of a pipet before the spin coater started to rotate for

5 s at 2000 rpm immediately followed by

90 s at 4000 rpm.

Although we did not apply explicitly a curing (baking) step of the final
sample after the preparation, the complete sample was baked for approximately
3 minutes at $\sim$ 140 ^{0}C to glue it with crystalbond 509 onto the ultrasonic
transducer of the sample. This was always done within 24 hours after the spin
coating procedure. We assume that, during this baking procedure, most of the
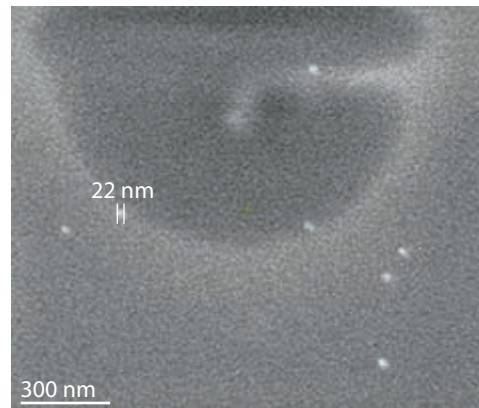remaining solvents in the sample were evaporated.

A AFM:
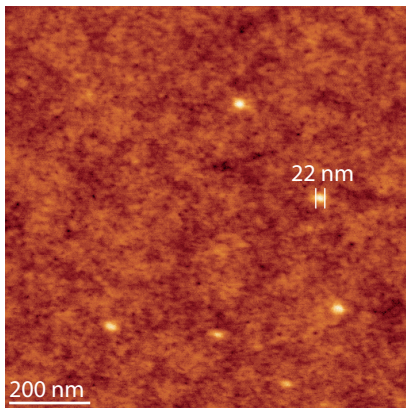
B SEM:

Figure 6.5: Density and distribution of the nanoparticles: (A) measured with an
AFM before burying them under an additional PVA layer, and (B) measured with a
SEM on the final sample, where the nanoparticles are covered by a 82 nm thick top
PVA layer.

6.B   Independent Verification of the Nanoparticle Depth

Rutherford Backscattering Spectrometry (RBS) is a technique that can quantitatively determine both the composition of a sample and the depth distribution of the elements [75]. The sample is bombarded with He-ions with a typical energy in the range of MeV. The He-ions are scattered at the atomic nuclei within the sample. An energy dependent histogram of the backscattered He-ions contains specific information on the type and depth of the atomic nucleus, at which the He-ion was scattered. Each element, or nucleus type, has its own distinct signature in an RBS spectrum. If a sample consists of a (very) thick layer of only one element, the energy at which the number of backscatter events drops to zero is called the surface channel. If the backscatter events of a certain element drop to zero at energies lower than the corresponding surface channel (surface signal shift), this particular element is covered by a layer of another element (of a composition of elements). The size of the shift is directly related to the thickness of the covering layer.

In order to quantify HFM experiments, it is of great importance to have a well defined sample, in which the depth of the subsurface particles (or features) is counterchecked with an independent technique. To this end, we performed an RBS measurement on the sample that we used for experiments, to quantify the exact depth of the gold nanoparticles as well as the thickness of the individual layers. To deduce quantitative data from an RBS measurement, it is necessary to perform a simulation [76]. Figure 6.6 shows both the RBS measurement (black) and the corresponding result of the simulation (red) [1]. The surface channels of the different elements in our sample (Carbon, Oxygen, Silicon, and Gold) are indicated in blue. Although almost at the detection limit of the RBS setup, the inset clearly shows a signal obtained from the buried gold nanoparticles: it is a sharp distribution, which indicates a well defined depth of the nanoparticles, with a clear shift away from the surface channel of Au, from which we can determine the thickness of the top PVA layer.

The RBS spectrum in Fig. 6.6 shows that Silicon is present just below the sample's surface, see the rise (and the tiny plateau) in the spectrum almost at the Silicon surface channel as well as layer 2 in Tab. 6.2. We can explain this with the presence of air bubbles in our sample and/or holes in some of the spin coated polymer layers. As a consequence, the best simulation result contains 4 layers on top of the Silicon wafer (see Tab. 6.2).
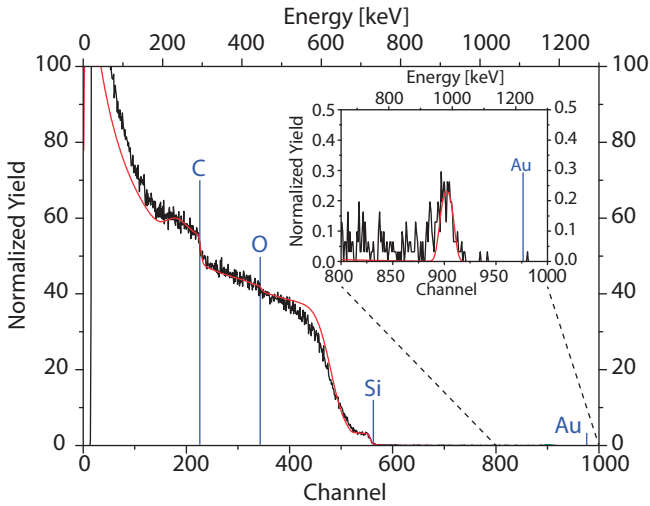
Figure 6.6: The RBS measurement (black) and the corresponding result of the simulation (red). The surface channel of the different elements in our sample (C, O, Si, and Au) are indicated in blue. Although almost at the detection limit of the RBS setup, the inset clearly shows a signal obtained from the buried gold nanoparticles.

layer	1	2	3	4	5
"material"	PVA	PVA	PVA	PMMA	Si
thickness [nm]	17	65	30	97	3000
density [10^{23} atoms/cm^3]	1.254	1.254	1.254	1.083	4.979
C	5.000	5.000	5.000	12.000	0.000
H	4.000	4.000	4.000	8.000	0.000
O	0.500	0.5000	0.500	1.000	0.000
Au	0.000	0.000	0.001	0.000	0.000
Si	0.000	0.430	0.430	0.800	1.000

Table 6.2: Layer thickness and composition according to our simulation that fit the RBS measurements best. Each layer is specified by its thickness [nm], its density [10^{23} atoms/cm^3], and its composition C:H:O:Au:Si (not normalized to 1, as this is performed automatically by the used software).

The combined thickness of layers 1 and 2 is 82 nm. Therefore, the gold nanoparticles are buried approximatly 82 nm below the surface. The thickness of the underlying PMMA layer is approximately 97 nm. We verified the total thickness of 209 nm by scanning over scratches on the sample with an AFM. The minimum thickness that we found in all AFM heightlines is ~ 250 nm, which confirms the RBS analysis.

It is striking that the sample contains more C than expected, but less O. From the simulation, we find the following composition for the PVA: $C_2H_{1.6}O_{0.2}$, which has to be compared to $C_2H_4O_1$. The lack of oxygen can be explained either by the formation of water during the baking procedure at ~ 140 degrees ^{0}C after the spin-coating or by a decomposition of the polymer layers during the RBS measurements (a clear spot on the sample surface was visible after the experiment). For the PMMA layer we find a composition of $C_5H_{3.3}O_{0.4}$ instead of $C_5H_8O_2$.

6.C   Cross Sections of the HFM Images at a Gold Nanoparticle

In this appendix, we provide typical cross sections of the height as well as the amplitude A_{diff} and the phase ϕ_{diff} of the heterodyne signal at a position of a gold nanoparticle for an applied contact force of 163 nN and 115 nN.

The cross sections at the nanoparticles taken for all channels of the HFM measurements at a contact force of 163 nN and 115 nN are shown in Fig. 6.7 and 6.8, respectively. The channels (and cross sections) belong to the height (A), the amplitude A_{diff} (B), the phase ϕ_{diff} (C), and (again) the height (D). All images also provide information on the values of the signal background next to the nanoparticles, since they all show raw data without filtering and background subtraction. The same pixel in the different channels were measured simultaneously. A, B, and C show the cross sections at the pixels indicated by the blue line, which is at the *exact same* location in A, B, and C. Please note that the blue line crosses the "middle" of the nanoparticle in B and C, whereas there is a clear offset in y- and also in x-direction in A. To capture the full height information we, therefore, added also images D, where the blue line is shifted over the "middle" of the nanoparticles.

At a contact force of 163 nN, all three channels clearly show a strong contrasts, whereas at 115 nN the contrasts in the subsurface channels B an C are almost of the same size as the corresponding background variations.
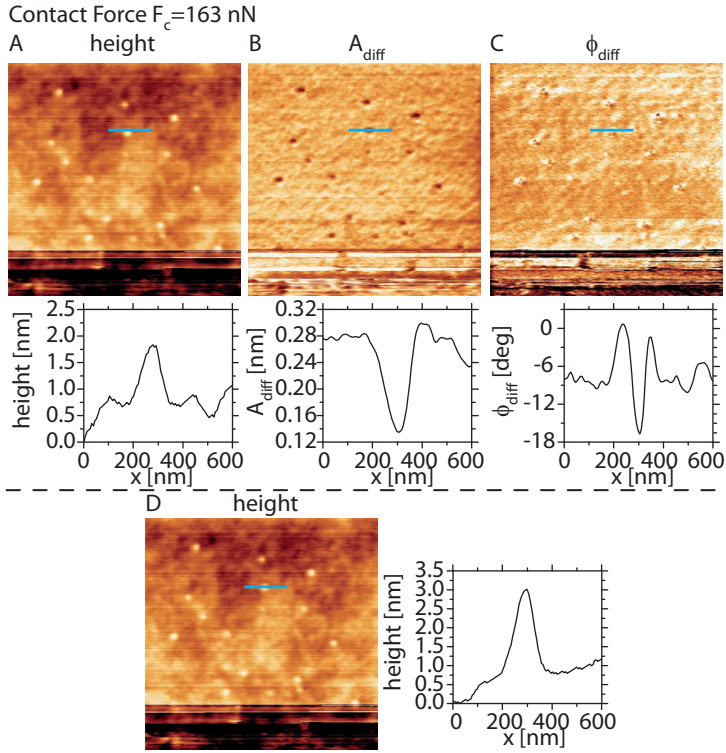
Figure 6.7: Cross sections at the nanoparticles taken for all channels of the HFM measurements at an applied contact force of 163 nN. The channels (and cross sections) belong to the height (A), the amplitude A_{diff} (B), the phase ϕ_{diff} (C), and (again) the height (D). All images are raw data without any filtering and also without any background subtraction such that the cross sections also provide information on the values of the signal background next to the nanoparticles. All channels are recorded simultaneously such that the same pixel in the different channels is taken at exactly the same time. A, B, and C show the cross sections at the pixels indicated by the blue line, which is at the *exact same* location in A, B, and C. It is remarkable that the blue line crosses the "middle" of the nanoparticle in B and C, whereas there is a clear offset in y- and also in x-direction in A. To capture the full height information we, therefore, added also image D, where the blue line is shifted over the "middle" of the nanoparticles. The cross sections are drawn over the same gold nanoparticle. $A_s + A_t = 1.71$ nm.
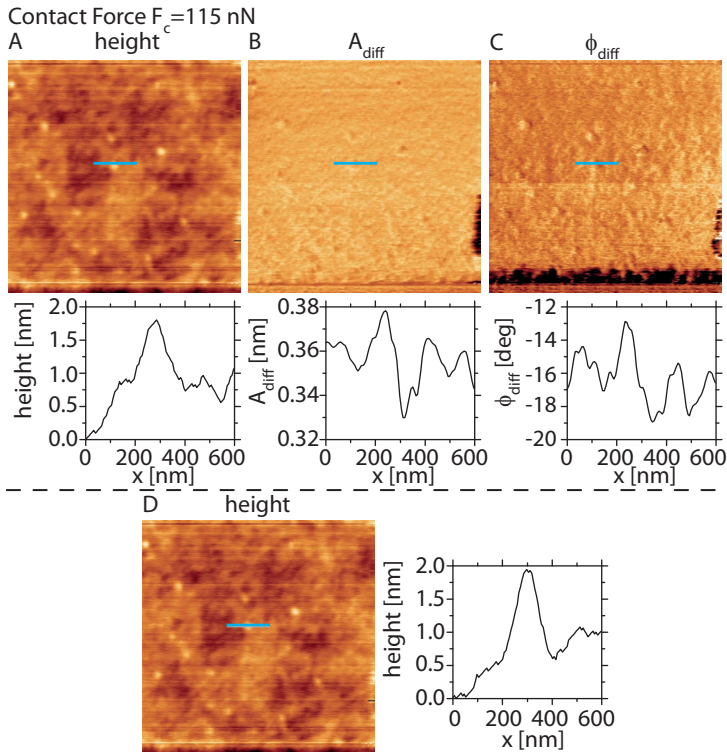
Figure 6.8: Cross sections at the nanoparticles taken for all channels of the HFM measurements at an applied contact force of 115 nN. The channels (and cross sections) belong to the height (A), the amplitude A_{diff} (B), the phase ϕ_{diff} (C), and (again) the height (D). All images are raw data without any filtering and also without any background subtraction such that the cross sections also provide information on the values of the signal background next to the nanoparticles. All channels are recorded simultaneously such that the same pixel in the different channels is taken at exactly the same time. A, B, and C show the cross sections at the pixels indicated by the blue line, which is at the *exact same* location in A, B, and C. It is remarkable that the blue line crosses the "middle" of the nanoparticle in B and C, whereas there is a clear offset in y- and also in x-direction in A. To capture the full height information we, therefore, added also image D, where the blue line is shifted over the "middle" of the nanoparticles. The cross sections are drawn over the same gold nanoparticle. $A_s + A_t = 1.71$ nm.

6.D   Experimental Dependence of the Difference Frequency Amplitude A_{diff} on the Sample Elasticity

To experimentally address the dependence of the amplitude A_{diff} of the heterodyne signal at the difference frequency on the elasticity of the sample, which is characterized by its Young's modulus E, we present results for the difference frequency generation on both a soft sample ($\sim$ 97 nm thick PMMA, $E \sim 2.4$ GPa) and a hard sample (Silicon (100) wafer, $E \sim 179$ GPa). The HFM experiment was performed with a similar cantilever as described in Sect. 6.2.

We obtained the Young's modulus on PMMA by fitting an experimentally obtained tip-sample interaction F_{ts} with the Derjaguin-Muller-Toporov (DMT-) model, see Sect. 1.4 and [23]. A parameter called λ, which is related to the elasticities of the tip and the sample, is usually used to differentiate between the applicabilities of different models that describe the tip-sample interaction, see Fig. 1.8 and [27]. As $\lambda = 0.63$ in our case, one should use the Maugis-Dugdale model [25]. Nevertheless, our approach with the DMT-model is fully justified, as we have demonstrated in Chap. 4 and in [52] that it does not matter at all for the numerical simulations which of the models describes the tip-sample interaction, as long as the fit perfectly matches the (experimentally obtained) tip-sample interaction. The only thing that matters is the particular shape (form) of $F_{ts}(z)$ and *not* the model that is used to describe this particular interaction.

The cantilever has a spring constant of 2.0 ± 0.4 N/m, which was calibrated using the thermal noise method [67]. We applied an *off-off* resonance excitation scheme with an ultrasonic tip frequency of 2.870 MHz and an ultrasonic sample frequency of 2.871 MHz leading to a heterodyne signal at a difference frequency f_{diff} of 1 kHz. The ultrasonic vibration amplitudes of both the tip A_t and the sample A_s were slightly different for the two experiments: $A_t = 0.94$ nm and $A_s = 0.32$ nm on Silicon, whereas $A_t = 1.23$ nm and $A_s = 0.18$ nm on PMMA. The tip amplitudes were determined using the procedure outlined in Sect. 5.E, in [52] and below we describe how we determined the sample amplitudes from the measurements. We measured the amplitude A_{diff} of the difference frequency as a function of the cantilever's base position z_b on both the Silicon and the PMMA layer. z_b is defined such that $z_b = 0$, if the deflection $\delta = 0$ during the approach cycle of the cantilever to the surface. This is exactly the point, at which the *effective* interaction (contact force) F_c on the tip changes sign from an attractive interaction to a repulsive interaction.

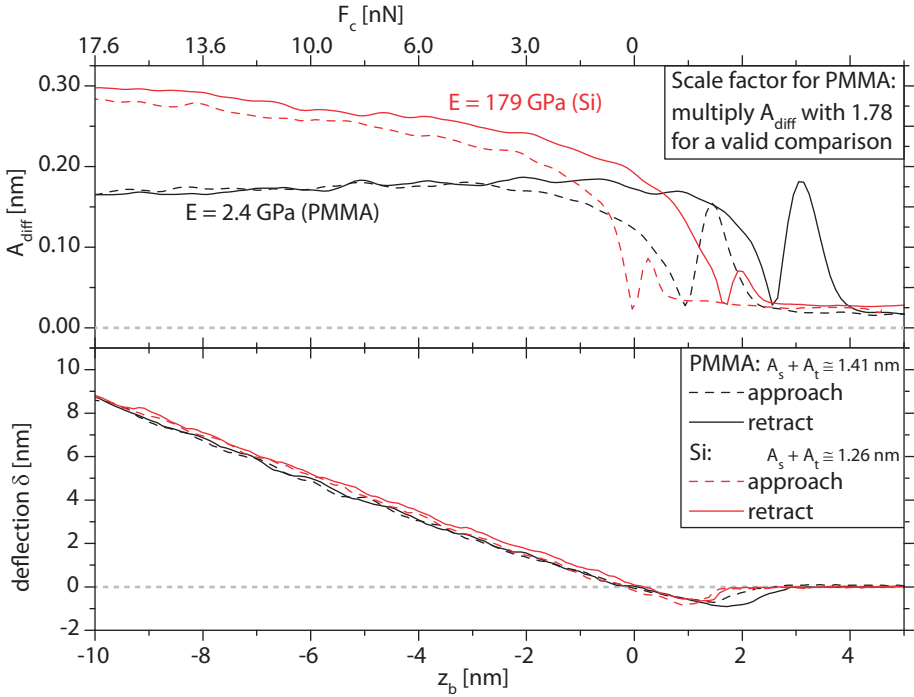Figure 6.9 shows the amplitude A_{diff} of the heterodyne signal as well as

Figure 6.9: Top panel: the amplitude A_{diff} of the heterodyne signal as a function of the cantilever's base position z_b on both a hard Silicon sample (red) and a soft PMMA layer (black). The top axis shows the contact force F_c for negative z_b. As $A_{\text{diff}} \propto A_s \cdot A_t / \sqrt{A_s^2 + A_t^2}$, see below, Chap. 5, and [69], and as the vibration amplitudes are slightly different for the measurements on Silicon and PMMA, one has to multiply the amplitude A_{diff} for the PMMA case with a scale factor of 1.78 to accommodate for a valid comparison. Please note that, even with this correction factor, A_{diff} is significantly larger on the hard Silicon surface (179 GPa) than on the soft ~ 97 nm thick PMMA layer (2.4 GPa). The lower panel shows the corresponding deflection δ of the cantilever.

the corresponding deflection of the cantilever as a function of the cantilever's base position z_b on both a Silicon sample (red) and a ~ 97 nm thick PMMA layer (black). The top axis in Fig. 6.9 shows the contact force F_c for negative z_b. To determine the ultrasonic vibration amplitude A_s of the sample, we can estimate A_s, for the case of Silicon, from the height of the plateau, using the method described in Chap. 4 and in [52], to be 0.32 nm. Without the existence of a clear plateau in the PMMA case (note the slight decrease of A_{diff} for negative z_b), we instead use the maximum amplitude of the difference frequency A_{diff} (0.18 nm) for the estimation and find $A_s = 0.18$ nm.

To enable a valid comparison between the measurements on the two different samples, one has to multiply the amplitude A_{diff} for the PMMA case with a correction factor of 1.78, as $A_{\text{diff}} \propto A_s \cdot A_t / \sqrt{A_s^2 + A_t^2}$ (see below, Chap. 5, and [69]) and as the vibration amplitudes are slightly different for the measurements on the different samples. Taking this correction factor into account, one still observes that, for the same contact force, A_{diff} is significantly larger on the hard Silicon surface than on the soft ~ 97 nm thick PMMA layer. The peaks in the attractive regime are larger for the soft PMMA sample, because the adhesion is larger on the PMMA sample than on the Silicon sample (please note the difference in deflection in the attractive part of the tip-sample interaction). Thus we conclude that the amplitude A_{diff} significantly depends on the elasticity of the sample and increases with increasing Young's modulus E.

6.E Analytical Dependence of the Difference Frequency Amplitude A_{diff} on the Sample Elasticity

The analytical theory that completely describes the generation of the heterodyne signal at the difference frequency for HFM experiments (see Chap. 5 and [69]) showed that the signal is characterized by the following analytical expressions:

$$A_{\text{diff}} e^{\text{i}\phi_{\text{diff}}} = \frac{A_s A_t}{\sqrt{A_s^2 + A_t^2}} \frac{I_2 e^{\text{i}(\phi_s - \phi_t)}}{|H^{-1}(\omega_{\text{diff}})| e^{\text{i}\Lambda} - I_1} \tag{6.1}$$

$$I_1 = \frac{1}{\pi} \int_{-1}^{1} \frac{\partial F_{ts}}{\partial z} \left(z_b + \delta + \sqrt{A_s^2 + A_t^2}\, u \right) \frac{du}{\sqrt{1 - u^2}} \tag{6.2}$$

$$I_2 = \frac{\sqrt{A_s^2 + A_t^2}}{2\pi} \int_{-1}^{1} \frac{\partial^2 F_{ts}}{\partial z^2} \left(z_b + \delta + \sqrt{A_s^2 + A_t^2}\, u \right) \sqrt{1 - u^2}\, du \tag{6.3}$$

, in which A_{diff} and ϕ_{diff} are the amplitude and the phase, respectively, of the signal at the difference frequency, and A_s and A_t are the ultrasonic vibration amplitudes of the sample and the tip with corresponding phases ϕ_s and ϕ_t. $|H^{-1}(\omega_{\text{diff}})|$ represents the absolute value of the inverse transfer function and its corresponding phase shift Λ, F_{ts} is the tip-sample interaction as a function of the tip-sample distance z, z_b is the position of the cantilever's base, and δ is the deflection of the cantilever.

The integrals I_1 and I_2 completely determine the generation of the signal at the difference frequency and they both depend on the particular tip-sample interaction F_{ts}. As the tip-sample interaction in the experiment can be well described by the Derjaguin-Muller-Toporov (DMT-)model [23], F_{ts} can be ex-

pressed by

$$
F_{ts}(z) = \begin{cases} -\dfrac{HR}{6a_0^2} + \dfrac{4}{3}E_f\sqrt{R}(a_0 - z)^{3/2} & \text{if } z \le a_0, \\[3mm] -\dfrac{HR}{6z^2} & \text{if } z > a_0. \end{cases} \tag{6.4}
$$

, in which R is the radius of the cantilever's tip, H the Hamaker constant, a_0 the distance at which the repulsive part of the tip-sample interaction is first felt by the cantilever ($\sim$ at the minimum of F_{ts}), and E_f is an effective Young's modulus describing the effective tip-sample stiffness. This effective Young's modulus E_f is determined by the elasticities (E_t and E) as well as the Poisson ratio's (μ_t and μ) of the cantilever and the sample, respectively:

$$
\frac{1}{E_f} = \frac{1 - \nu^2}{E} + \frac{1 - \nu_t^2}{E_t} \tag{6.5}
$$

Since we probe our final sample that consists of several polymers layers, of which $E \sim 2.4$ GPa, with a hard Silicon cantilever with $E_t \sim 179$ GPa, we can neglect $(1 - \nu_t^2)/E_t$ and receive that the effective elasticity E_f is directly proportional to the elasticity E of the sample. The repulsive part of the tip-sample interaction, see Eq. 6.4, is, therefore, also directly proportional to the elasticity E of the sample. As a consequence, this is valid also for the integrals I_1 and I_2 described by Eqs. 6.2 and 6.3. Using these proportionality relations in Eq. 6.1, we find a simple expression for the elasticity dependence of the amplitude A_{diff} of the heterodyne signal:

$$
A_{\text{diff}} \propto \left| \frac{E}{\gamma + E} \right| = \frac{E}{\sqrt{E^2 + |\gamma|^2 + 2E\,\mathrm{Re}\,[\gamma]}} \tag{6.6}
$$

, in which γ is a complex constant. If the cantilever is completely in the Hertzian contact regime ($z < a_0$) during its oscillation, gamma can be written as

$$
\gamma = \frac{|H^{-1}(\omega_{\text{diff}})|e^{i\Lambda}}{\left[\dfrac{2\sqrt{R}\sqrt{A_s^2 + A_t^2}}{\pi} \right] \displaystyle\int_{-1}^{1} \sqrt{\dfrac{\alpha - u}{1 - u^2}}\, du} \tag{6.7}
$$

, in which α is the normalized indentation given by:

$$
\alpha = \frac{a_0 - z_b - \delta}{\sqrt{A_s^2 + A_t^2}} \tag{6.8}
$$

We can evaluate an lower estimate for γ by setting the normalized indentation $\alpha = 1$ and noticing that for smaller α, the integral in the expression for

γ would become smaller, and γ, therefore, larger. Using the ultrasonic ampli-
tudes of both the tip and the sample, we appraise $\sqrt{A_s^2 + A_t^2} = 1.39$ nm. For
the tip radius we assume $R = 5$ nm. The inverse transfer function $|H^{-1}(\omega_{\text{diff}})|$
can be derived as described in Sect. 5.B and in [69], in which we take a spring
constant of 2.5 N/m and set Λ to zero. This leads to the following estimates
for γ and A_{diff}:

$$\gamma = 0.5\,\text{GPa}$$

$$A_{\text{diff}} \propto \frac{E\,[\text{in GPa}]}{0.5 + E\,[\text{in GPa}]} \qquad (6.9)$$

, in which E has to be inserted in GPa. Equation 6.9 describes an analytical
dependence of A_{diff} on the sample elasticity E. For soft samples, in which E
is smaller than 0.5 GPa, A_{diff} is approximately proportional to E. Therefore,
we also expect analytically that a harder sample results in a higher amplitude
A_{diff} of the heterodyne signal, especially above the nanoparticles, where the
effective elasticity is slightly increased with respect to the soft polymer. On
very hard samples, with $E \gg 0.5$ GPa, A_{diff} approaches a constant value and
becomes independent of E.

Please note that we have neglected the influence of the elasticity on both the
deflection of the cantilever and the transfer function of the cantilever. However,
this is a valid approximation, as we never saw a decrease in the amplitude A_{diff}
of the difference frequency at a given contact force while the elasticity E of the
sample was increased.

6.F   Effective Sample Elasticity above the Nanoparticles

In this appendix, we derive an upper bound for the effective sample elas-
ticity, measured at the sample surface, that is increased by the presence of the
buried nanoparticles in the polymer.

Figure 6.10 shows a schematic cross section of the sample, which consists of
a PVA layer (PVA), the gold nanoparticles (Au), and a PMMA layer (PMMA).
The Au is buried at the depth d, and has a radius R. The total thickness of
the sample is denoted with t. The sample is compressed by a stress σ, which
is equal to the force F per unit area A.

From linear elasticity theory, we know that an applied external stress is
negatively proportional to the relative change in thickness, in which the pro-
portionality factor is given by the Young's modulus E of the material. For our
sample this reduces to the following equations:

$$\sigma = -\frac{E_{PVA}}{d - R}(\delta d - \delta R) = -\frac{E_{Au}}{2R}(2\delta R) = \frac{E_{PMMA}}{t - d - R}(\delta t - \delta d - \delta R) \qquad (6.10)$$
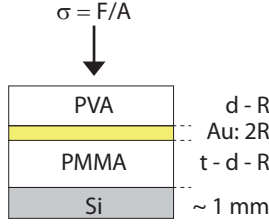
Figure 6.10: A schematic cross section of the sample, which consists of a PVA layer (PVA), the gold nanoparticle (Au), and a PMMA layer (PMMA). The Au is buried at the depth d, and has a radius R. The total thickness of the sample is denoted with t. The sample is compressed by a stress σ, which is equal to the force F per unit area A.

, in which E_{PVA}, E_{Au}, and E_{PMMA} are the Young's moduli of PVA, gold, and PMMA, respectively, δd is the variation in depth of the nanoparticle, δR is the variation in radius of the nanoparticle, and δt is the variation in thickness of the sample.

It is straightforward to derive the solutions for δd, δR, and δt, from Eq. 6.10:

$$\delta d = -R\sigma \left[E_{Au}^{-1} - E_{PVA}^{-1} \right] - d\sigma E_{PVA}^{-1} \tag{6.11}$$

$$\delta R = -R\sigma E_{Au}^{-1} \tag{6.12}$$

$$\delta t = -t\sigma E_{PMMA}^{-1} - d\sigma \left[E_{PVA}^{-1} - E_{PMMA}^{-1} \right]$$
$$- R\sigma \left[2E_{Au}^{-1} - E_{PVA}^{-1} - E_{PMMA}^{-1} \right] \tag{6.13}$$

If one introduces an effective Young's modulus E_{eff}, the complete sample with all three layers can be regarded also as a sample consisting of one layer with a thickness t of an isotropic material such that

$$\sigma = -\frac{E_{eff}}{t} \delta t \tag{6.14}$$

By substituting Eq. 6.13 in Eq. 6.14, we find an expression for the effective Young's modulus E_{eff}:

$$E_{eff} = \frac{1}{E_{PMMA}^{-1} + \frac{d}{t} \left[E_{PVA}^{-1} - E_{PMMA}^{-1} \right] + \frac{2R}{t} \left[E_{Au}^{-1} - 0.5E_{PVA}^{-1} - 0.5E_{PMMA}^{-1} \right]} \tag{6.15}$$

Let us now discuss the two limits of this equation. Firstly, if the diameter $2R$ of the nanoparticle is equal to the thickness t of the sample (and thus $d = 0$), we find that $E_{eff} = E_{Au}$. Secondly, if the radius R of the nanoparticle is equal

to zero and the sample is infinitely thick ($t \gg d$), we find that $E_{eff} = E_{PMMA}$. Thirdly, if the radius R of the nanoparticle is equal to zero and $d = t$, we find that $E_{eff} = E_{PVA}$. These results reflect correct expectations, as the sample consists only of Au in the first case, only of PMMA in the second case, and only of PVA in the third case.

Equation 6.15 provides an upper bound on the elasticity on the surface above a nanoparticle. In reality, the variation in elasticity due to a nanoparticle should be derived from a 3D calculation, as the stress is spread out also laterally through the sample [77]. As a consequence, the rise in elasticity caused by the presence of the nanoparticle decreases with increasing depth of the nanoparticle. This effect is comparable to a stone underneath a pillow: if one just touches the pillow, the stone is not felt, but if one pushes harder into the pillow, the presence of the stone is clearly noticed.

Let us now calculate the expected effective elasticity increase for our samples. PMMA and PVA, both have a similar Young's modulus: $E_{PMMA} \sim E_{PVA} = 2.4$ GPa. Under this assumption, Eq. 6.15 reduces to:

$$E_{eff} = \frac{1}{E_{PVA}^{-1} + \frac{2R}{t} \left[E_{Au}^{-1} - E_{PVA}^{-1} \right]} \tag{6.16}$$

We assume that the Young's modulus of the gold nanoparticle is equal to that of bulk gold, which is 78 GPa [78] and consider the total thickness to be $t = 209$ nm. For the radius, we take $R = 10$ nm of the gold nanoparticles, as this is the average of their radii distribution [73, 74]. Using this value for the radius R, we find the effective Young's modulus E_{eff} to be equal to 2.65 GPa. Therefore, the surface directly above the nanoparticle has (at maximum) a 10% higher Young's modulus than that of the bulk polymer of 2.4 GPa.

6.G   Setting up the Numerical Calculations

As the amplitude and phase contrast highly depend on both the exact excitation scheme and precise resonance frequency spectrum of the cantilever, which can even result in a contrast inversion, it is of uttermost importance to match the spectrum of the cantilever in the numerical calculation (numerical cantilever) to the spectrum of the cantilever used in the experiment (experimental cantilever). In this appendix, we describe the matching procedure.

On the basis of the resonance frequencies f_i^{num} of the numerical cantilever and the corresponding resonance frequencies f_i^{exp} of the experimental cantilever, we defined a normalized, relative error e_i for each resonance frequency:

$$e_i = \frac{|f_i^{num} - f_i^{exp}|}{f_i^{exp}} \tag{6.17}$$

We took into account the first 5 modes of the cantilever and used the average e_i as a measure for the quality of our fit. We optimized the fit by varying the elasticity E_t of the cantilever, the length L of the cantilever, the tip mass m_e, the moment of inertia I_e of the tip, and the density ρ_s of the cantilever. As a best fit, with an average error of 1.397%, the cantilever is described by following parameters: $E_t = 222$ GPa, $L = 207$ μm, $m_e = 5.76 \cdot 10^{-15}$ kg, $I_e = 3.51 \cdot 10^{-22}$ kg m^2, and $\rho_s = 3207$ kg m^{-3}. We did not fit the width and the thickness of the cantilever. Instead we have chosen them to be 20 μm and 2.7 μm, respectively, to set the spring constant of the numerical cantilever to 2.5 N/m such that it is comparable to the spring constant of 2.7 ± 0.4 N/m of the experimental cantilever.

The Q-factors that describe the widths of the resonance peaks, were chosen such that the widths of the resonance peaks match between the numerical and the experimental cantilever. If Q_i^{exp} is the experimentally measured Q-factor of the resonance frequency f_i^{exp}, the corresponding numerical Q-factor Q_i^{num} is related to Q_i^{exp} by

$$Q_i^{num} = \frac{f_i^{num}}{f_i^{exp}} Q_i^{exp} \tag{6.18}$$

Fig. 6.11 shows the vibration spectrum of both the experimental cantilever and the numerical cantilever. The bottom two panels show the amplitude and the phase of the experimental cantilever. The phase extremely decreases almost linear with the frequency (notice the phase change from 0^0 to -4200^0): this is due to the phase change in the fixed cables, which deliver the electronic drive signal to the cantilever. The red lines indicate the experimentally determined resonance frequencies, which are indicated at the top together with their corresponding Q-factors that describe the widths of the resonance peaks. The second panel from the top shows the spectrum of the numerical cantilever. The blue lines indicate the frequencies of this particular excitation scheme with $f_t = 2.50$ MHz (cantilever) and $f_s = 2.52$ MHz (sample), as well as the difference frequency $f_{\text{diff}} = 20$ kHz.
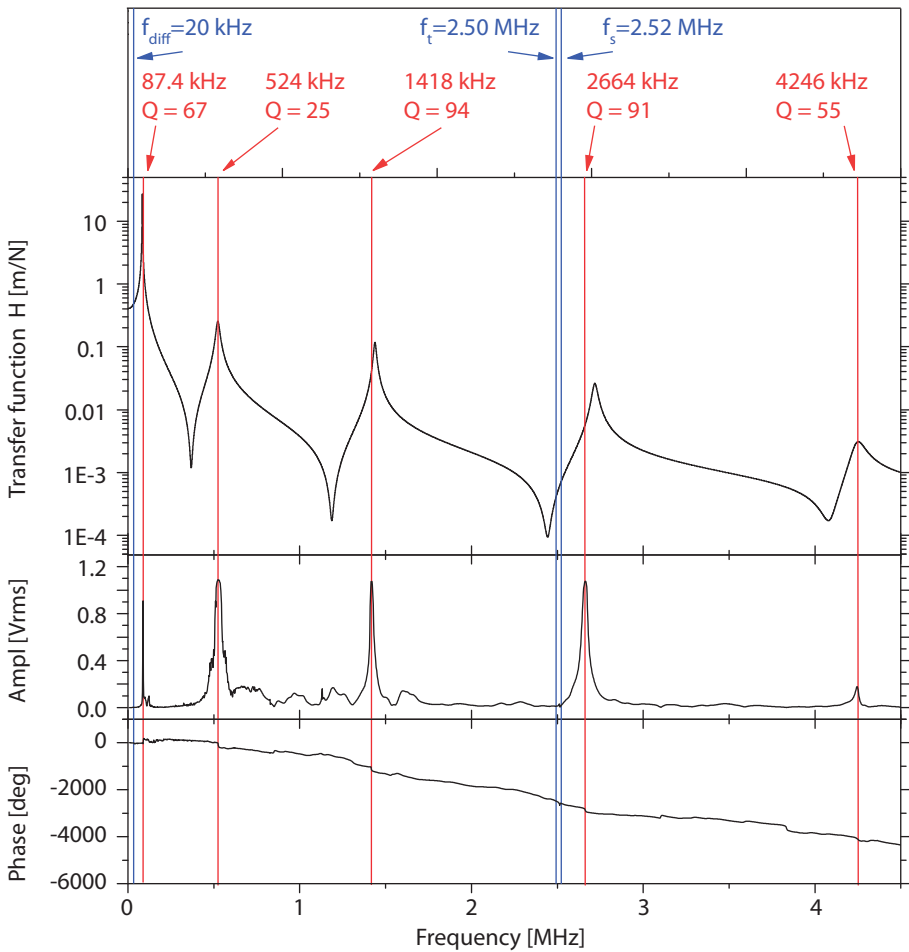
Figure 6.11: The vibration spectrum of both the *experimental* and the *numerical* cantilever. The bottom two panels show the amplitude and the phase of the experimental cantilever. The phase extremely decreases almost linear with the frequency (notice the phase change from 0^0 to -4200^0): this is due to the phase change in the fixed cables, which deliver the electronic drive signal to the cantilever. The red lines indicate the experimentally determined resonance frequencies, which are indicated at the top together with their corresponding Q-factors that describe the widths of the resonance peaks. The second panel from the top shows the spectrum of the numerical cantilever for comparison. The blue lines indicate the frequencies of this particular excitation scheme with $f_t = 2.50$ MHz (cantilever) and $f_s = 2.52$ MHz (sample), as well as the difference frequency $f_{\text{diff}} = 20$ kHz.

6.H   Complete Overview of the Results of the Numerical Calculations

In Sect. 6.3, we describe the results of three different schemes for the ultrasonic excitations: *off-off resonance*, in which the ultrasonic excitations are chosen halfway between the 3rd and 4th resonance of the cantilever; *off-on resonance*, in which the ultrasonic excitation frequencies are on the 4th resonance of the cantilever; *experimental excitation*, in which the ultrasonic excitation frequencies are equally far away from the nearest resonance frequency as in the experiment. In this appendix, we present the full numerical results of both the *off-off resonance* and the *off-on resonance* scheme.

Figure 6.12 shows the results for the *off-off resonance* excitation scheme. The top panel shows the vibration spectrum: blue lines indicate the excitation frequencies and red lines the resonance frequencies. The bottom three panels show the numerical results for different sample elasticities as a function of the applied contact force F_c (given by I_0): 2 GPa (black), 3 GPa (red), 4 GPa (magenta), 5 GPa (green), and 6 GPa (blue). The panels depict from left to right the indentation ($\sim$ inverted height), the amplitude A_{diff}, and the phase ϕ_{diff}. The cantilever's motion is unstable for some contact forces while indenting in the sample (see jumps at $\sim$ 70 nN). Note that after the instability the motion is stable again, A_{diff} is smooth, we receive smooth motions of the cantilever, and the phase differences approach values that correspond to the numerical error of the lock-in.

Let us first discuss the instabilities in the motion of the cantilever. As these instabilities also appear in the retract curves (not shown here) at approximately the same contact forces as in the approach curves, it indicates that they are *not* based on a numerical issue (instability) within the simulation. Please note also that, with increasing contact force, we receive smooth motions of the cantilever after the instabilities, which is a second indication that it is not based on a numerical issue. The instabilities must be real. With increasing contact force, the resonance frequencies of the cantilever shift towards higher frequencies [79]. As a consequence, the value of the transfer function of the cantilever at the ultrasonic tip frequency $H(f_t)$ increases, see Fig. 6.12. Therefore, the ultrasonic tip amplitude A_t rises, which also results in an increase of A_{diff}, see Eq. 6.1 above. This leads to an even deeper penetration of the tip into the sample, which, in turn, results in a further shift of the resonance frequencies towards higher frequencies. This feedback mechanism leads to the instabilities, as the amplitude of the ultrasonic tip motion of the cantilever keeps increasing.

The increase in amplitude has a counterintuitive effect on the indentation, which is shown in Fig. 6.13. The red region indicates the initial cantilever oscillation. If the vibration amplitude of the cantilever increases, as indicated with the blue region, the cantilever penetrates deeper into the sample, see 1 in
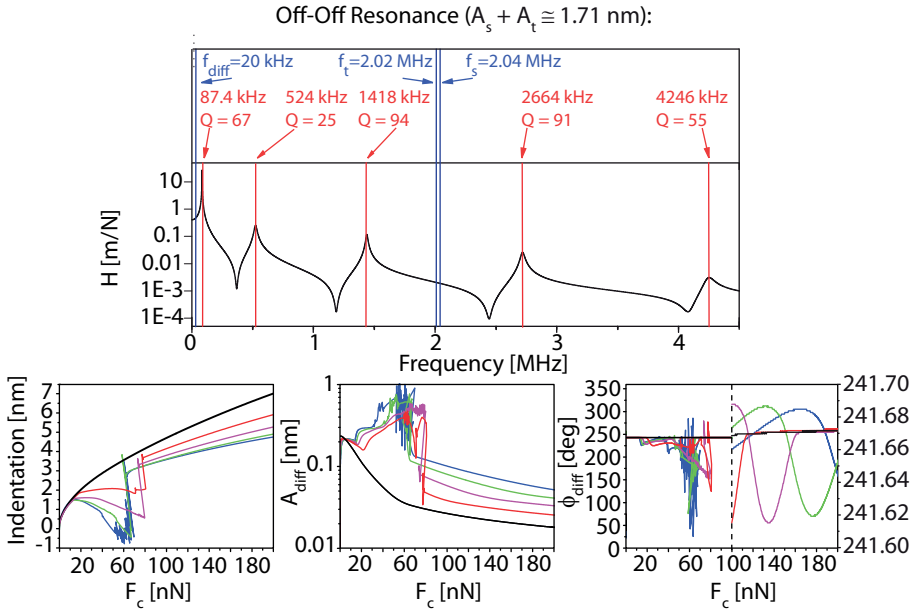
Figure 6.12: The top panel shows the vibration spectrum in the *off-off resonance* scheme: blue lines indicate the excitation frequencies, whereas red lines indicate the resonance frequencies of the cantilever. The bottom three panels show the numerical results of the *off-off resonance* scheme for different sample elasticities as a function of the applied contact force F_c (given by I_0): 2 GPa (black), 3 GPa (red), 4 GPa (magenta), 5 GPa (green), and 6 GPa (blue). The panels display from left to right the indentation ($\sim$ inverted height), the amplitude A_{diff}, and the phase ϕ_{diff}. We observe an instability in the cantilever's motion while indenting into the sample (see jumps at $\sim$ 70 nN). Note that, after the instabilities, we receive smooth motions of the cantilever and the phase differences approach values that correspond to the numerical error of the lock-in.

Fig. 6.13. This results in a larger than linear increase of the average force on the cantilever during one oscillation, as the tip-sample interaction is *nonlinear*. To compensate for this additional increase in average force, the equilibrium position of the cantilever shifts, see 2 in Fig. 6.13, which results in a *decrease* of the indentation. The equilibrium positions of the cantilever are indicated by the dashed lines. It is exactly this effect that we observe in Fig. 6.12 for contact forces between 15 nN and 85 nN. Since the cantilever is moved continuously into sample during the approach phase, the instability can only arise, if the decrease in indentation per unit time is larger than the speed at which the cantilever is pushed into the sample. Note that the instability does not remain. During the
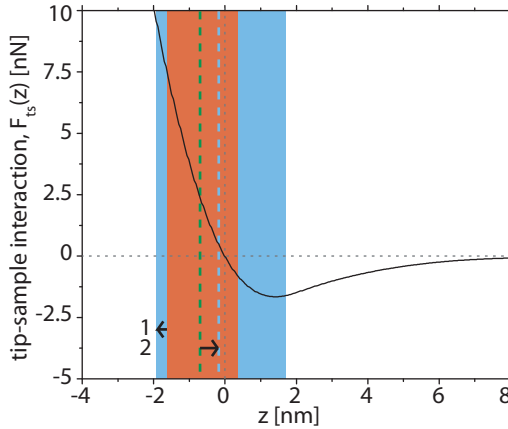
Figure 6.13: Graph that shows that there is a *decrease* of the indentation, if the (ultrasonic) vibration amplitude of the cantilever *increases*. Initially, the cantilever is oscillating in the region that is indicated in red. If the vibration amplitude increases, as indicated with the blue region, the cantilever penetrates deeper into the sample during its oscillation (1). Since the tip-sample interaction is *nonlinear*, this results in a larger than linear increase of the average force on the cantilever during one oscillation. Consequently, the equilibrium position of the cantilever shifts (2), which results in a *decrease* of the indentation. The equilibrium positions are indicated with the dashed lines.

decrease of the indentation, the integral I_2, which determines the amplitude at the difference frequency (see Eq. 6.1), also starts to decrease. When the cantilever starts to probe the attractive part of the tip-sample interaction, the integral I_2 even rapidly decreases to zero. At this moment, the cantilever quickly shoots back into the sample to find its new equilibrium position: the cantilever snaps into contact with the surface [79]. During this process, the cantilever has no time to enter again the instability loop. We find evidence for this behavior in the indentation shown in Fig. 6.12: the indentation decreases after an initial maximum with increasing contact force, until it snaps back into the sample at the position of the instability.

Figure 6.14 shows the results for the *off-on resonance* excitation scheme. The top panel shows the vibration spectrum: blue lines indicate the excitation frequencies and red lines the resonance frequencies. The bottom three panels show the numerical results for different sample elasticities as a function of the applied contact force F_c (given by I_0): 2 GPa (black), 3 GPa (red), 4 GPa (magenta), 5 GPa (green), and 6 GPa (blue). The panels depict from left to right the indentation ($\sim$ inverted height), the amplitude A_{diff}, and the phase ϕ_{diff}.
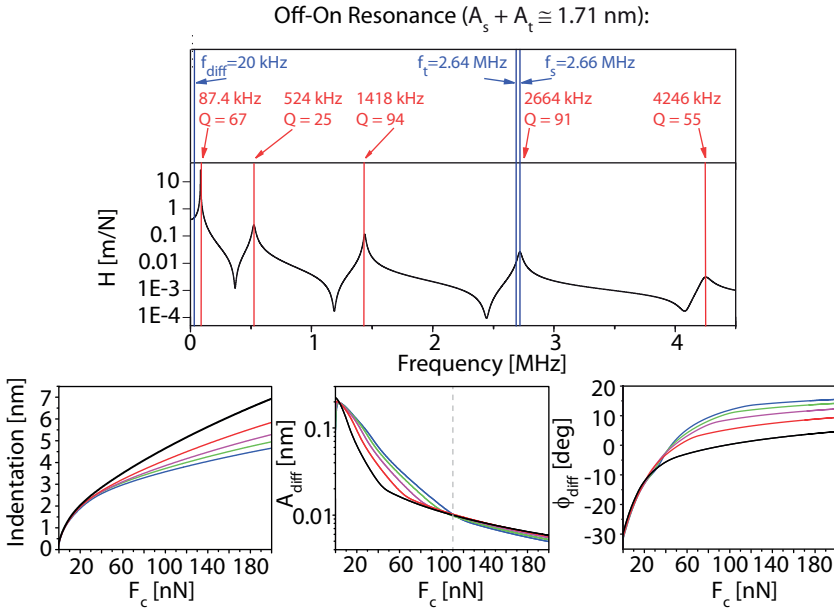
Figure 6.14: The top panel shows the vibration spectrum in the *off-on resonance* scheme: blue lines indicate the excitation frequencies, whereas red lines indicate the resonance frequencies of the cantilever. The bottom three panels show the numerical results of the *off-on resonance* scheme for different sample elasticities as a function of the applied contact force F_c (given by I_0): 2 GPa (black), 3 GPa (red), 4 GPa (magenta), 5 GPa (green), and 6 GPa (blue). The panels display from left to right the indentation ($\sim$ inverted height), the amplitude A_{diff}, and the phase ϕ_{diff}.

This time, we do not observe any instabilities, as the value of the transfer function of the cantilever decreases with the shifting of the resonance frequencies towards higher frequencies. This is also the reason, why we do not see an instability in the results of the *experimental excitation* scheme, which is presented in Fig. 6.3. Let us, in the following, have a closer look to the implications on the contrasts, if applying a the specific excitation scheme.

We start with the height contrast. In both the *off-off resonance* and the *off-on resonance* excitation scheme, we observe that a softer sample (2 GPa) leads to a deeper indentation at a given contact force. Since we consider measurements that are performed with the feedback operating in contact mode, the contact force is held constant and a variation in elasticity results in different indentations, which translates into a measurable height signal: a harder material appears to be higher. This consideration holds for all excitation schemes

including also the *experimental excitation* scheme, as discussed in Sect. 6.3.

Considering the contrast in the amplitude A_{diff} that results from parts of the sample with different elasticities, we observe opposite behavior between the *off-off resonance* scheme and the *off-on resonance* scheme. In the *off-off resonance* excitation scheme, we see that a hard surface leads to a higher amplitude A_{diff} than a soft surface. This additionally supports both the experimental results of Appx. 6.D and the analytical result of Appx. 6.E. In contrast, in the *off-on resonance* excitation scheme, we observe that for large contact forces (> 110 nN, see Fig. 6.14), a soft surface generates a higher amplitude A_{diff} than a hard one. We trust this result of our simulation at large contact forces, as the cantilever is completely vibrating in the Hertzian contact regime of the tip-sample interaction at these contact forces: the cantilever does not feel any attractive forces during is motion. This is not the case at lower forces (< 110 nN), where the contrast is inverted. Further evidence for a contrast inversion as a function of the applied contact force comes from the fact that the retract curves (not shown here) show exactly the same characteristics. The contrast inversion between the *off-on resonance* case and the *off-off resonance* case is caused by the frequency shift of the 4th resonance frequency of the cantilever, which is explicitly excited in the *off-on resonance* excitation scheme. We will discuss this amplitude inversion in Appx. 6.I in more detail.

Let us finish with the variations in the phase that result from parts of the sample with different elasticities. The phase ϕ_{diff} is directly related to the shift of that resonance frequency that is nearest to the ultrasonic excitation of the tip, as will be discussed in Appx. 6.I. In the *off-off resonance* excitation scheme, we observe phase variations in the order of 10 millidegrees between a hard and a soft surface. After the initial phase oscillations, which are inherently connected to the instabilities, the phase variations become smaller and reduce finally to a millidegree. In the *off-on resonance* scheme, the phase variations between a hard and a soft surface are in the order of a few degrees. We provide an explanation for the huge difference in sensitivity on the phase in the next appendix.

6.I Frequency Shifts and their Consequences for the Contrasts

In Sect. 6.3 as well as in Appx. 6.H, we argued that both the observed amplitude and the phase contrast are related to a shift of the resonance frequencies, especially in the *off-on resonance* excitation scheme. We even show that the amplitude contrast can be inverted depending on the applied excitation scheme. In this appendix, we consider the effect on the contrasts based on a shift of the 4th resonance frequency of the cantilever to highlight the implications on the contrasts.
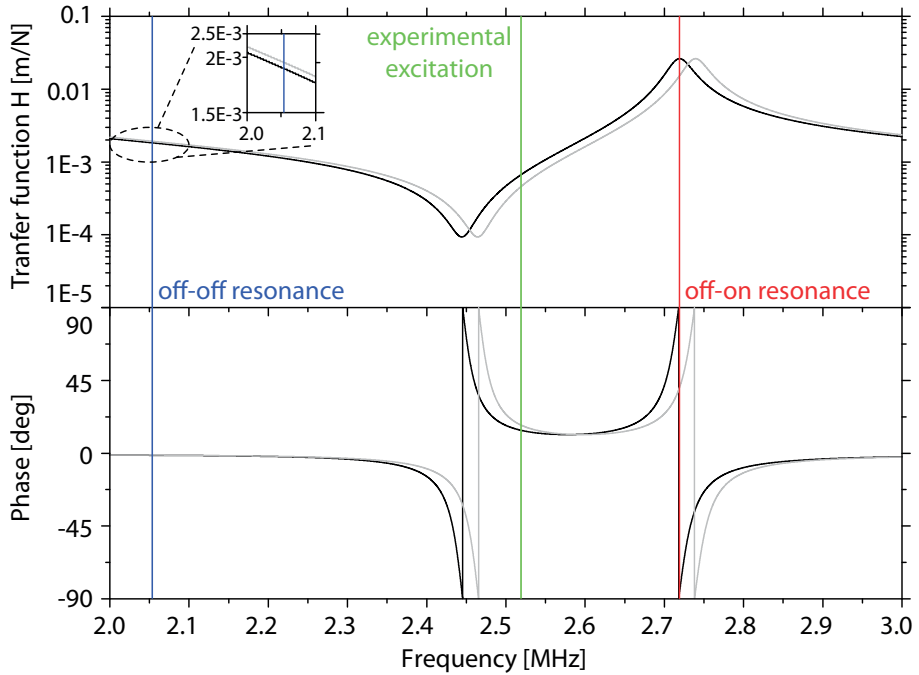
Figure 6.15: The top panel shows the transfer functions of the cantilever used in our calculations around its 4th resonance frequency and the bottom panel shows the corresponding phases. The black line shows the vibration spectrum of the *free* hanging cantilever, while the gray line shows the spectrum of the cantilever, when it is pushed with a contact force of 670 nN into a sample with an elasticity of $E = 2$ GPa. The three vertical lines represent the ultrasonic tip excitation frequencies applied in the different excitation schemes: *off-off resonance* (blue), *experimental excitation* (green), and *off-on resonance* (red). The corresponding ultrasonic sample excitations cannot be drawn in the current graph, as they are chosen in our experiment to be only 20 kHz lower than the ultrasonic tip excitations. The inset shows that the transfer function increases in the *off-off resonance* scheme, when the cantilever is pushed into a sample.

Let us first address the shifting of the resonance peaks in general. For small vibration amplitudes, the frequency shifts are proportional to $-\partial F_{ts}/\partial z$ [79]. This implies that in the attractive regime ($z > a_0$) all resonance frequencies shift towards lower frequencies for the particular tip-sample interaction described by Eq. 6.4. On the other hand, all resonance frequencies shift towards higher frequencies in the repulsive Hertzian contact regime ($z < a_0$). Considering the magnitude of the shifts, we note that, in the repulsive Hertzian contact regime, $\partial F_{ts}/\partial z$ is proportional to the elasticity E of the sample. Therefore,

the shifts of the resonance frequencies are larger on a hard sample than on a soft one.

The top panel in Fig. 6.15 shows the transfer functions of the cantilever used in our numerical calculations around its 4th resonance frequency and the bottom panel shows the corresponding phases. The black line depicts the vibration spectrum of the *free* hanging cantilever, while the gray line shows the shifted spectrum, when the cantilever is pushed with a contact force of 670 nN into a sample with an elasticity of $E = 2$ GPa. The three vertical lines represent the ultrasonic tip excitation frequencies that are applied in the different excitation schemes: *off-off resonance* (blue), *experimental excitation* (green), and *off-on resonance* (red). The corresponding ultrasonic sample excitations are not shown in the current graph, as they are chosen by default (in our case) to lie only 20 kHz below the ultrasonic tip excitations.

In the following, it is important to notice that, in all three excitation schemes, the excitation force on the tip at the excitation frequency is held constant. Figure 6.15 shows that, for both the *off-on resonance* and the *experimental excitation* scheme, a shift of the resonance frequency towards higher frequencies results in a decrease of the value of the transfer function. As a consequence, the resulting ultrasonic tip amplitude A_t is decreased. This implies that also the amplitude A_{diff} is decreased, as $A_{\mathrm{diff}} \sim A_s \cdot A_t / \sqrt{A_s^2 + A_t^2}$, see Eq. 6.1. The decrease of the transfer function is accompanied by a phase shift. Following the same line of reasoning, this phase shift translates into a shift of the phase ϕ_{diff}.

The described effects hold for *all* excitations of the cantilever, including also the excitation at the heterodyne difference frequency. This leads to a variety of excitation schemes with different sensitivities and contrasts. Keeping this in mind, we can now consider the effects of local elasticity variations of the surface on both the amplitude A_{diff} and the phase ϕ_{diff} of the signal at the heterodyne difference frequency in Heterodyne Force Microscopy.

Let us first discus the amplitude contrast ΔA_{diff} for the *off-on resonance* and *experimental excitation* scheme. In both schemes, we observed that the value of the transfer function decreases, if the resonance frequencies shift towards higher frequencies when the cantilever gets into contact with the sample. As the size of the shifts are proportional to the elasticity E of the sample, the resonance frequencies shift *more* on a hard part of the surface than on a soft part. This results in a *lower* value of the transfer function on the hard parts of the surface implying that also the ultrasonic tip amplitude A_t and, consequently, also the amplitude A_{diff} are *lower* on the hard parts of the surface. Effectively, this can result in a *negative* amplitude contrast ('holes' in A_{diff} at the position of the nanoparticles), which matches our observations described in Sect. 6.2 for the *off-on resonance* excitation scheme. However, there is also a counter effect: A_{diff} is larger on harder parts of the sample, as the amplitude $A_{\mathrm{diff}} \sim E$ (see

Appxs. 6.D and 6.E). Therefore, if an increase in E (and therefore in A_{diff}) overcompensates the decrease in A_t, it is still possible to observe, like in the *experimental excitation* schemes, a *positive* amplitude contrast ΔA_{diff}.

In the *off-off resonance* excitation scheme, the value of the transfer function increases, if the resonance frequencies shift towards higher frequencies when the cantilever gets into contact with the sample (see the inset in Fig. 6.15). Therefore, both the ultrasonic tip amplitude A_t and the amplitude A_{diff} are *higher* on a hard part of the surface. The increase in amplitude A_{diff} is even magnified by the increase of A_{diff} due to the higher Young's modulus E. Therefore, we always observe a *positive* amplitude contrast in the *off-off resonance* scheme.

Considering the variations in the phase that result from parts of the sample with different elasticities, the bottom panel of Fig. 6.15, which shows the phase of the transfer function, serves as a starting point. In analogy to the amplitude contrast, the contrast in the phase ϕ_{diff} is defined by the difference between ϕ_{diff} on a hard part of the surface and on a soft part. Equation 6.1 shows that $\phi_{\mathrm{diff}} = \phi_t + const$, in which we neglected the phase Δ of the transfer function at the difference frequency. This is a valid assumption, since we have chosen the difference frequency to be $f_{\mathrm{diff}} = 20$ kHz in both our HFM experiments and the simulations, while the first resonance frequency of the cantilever is at 87.4 kHz. As a consequence, the phase ϕ_{diff} is determined by the phase ϕ_t of the ultrasonic cantilever motion.

The sensitivity of the phase ϕ_t to a shift of the resonance frequency, is determined by $\partial\phi_t/\partial f$. This function has a strong maximum at a resonance frequency of the cantilever. As a result, the phase ϕ_t in the *off-on resonance* scheme is extremely sensitive to small frequency shifts. This sensitivity decreases, if the ultrasonic cantilever excitation is further away from a resonance frequency of the cantilever. Therefore, the *experimental excitation* scheme is less sensitive for a variation in ϕ_t (and therefore ϕ_{diff}), than the *off-on resonance* scheme, but more sensitive than the *off-off resonance* scheme. As argued above, the magnitude of the frequency shift is proportional to the Young's modulus of the surface. The explained phase sensitivity is the reason why the phase contrast is in the order of ten degrees for the *off-on resonance* excitation scheme, decreases to one degree in the *experimental excitation* scheme, before it almost vanishes in the *off-off resonance* excitation scheme.